Large-eddy simulations of nearshore offshore wind farms and their interactions with atmospheric boundary layer

Jay Prakash Goit

Department of Mechanical Engineering, Kindai University

1. Introduction

Many countries around the world have set ambitious targets for renewable energy and have planned phase-out of fossil-fuel based energy generation. In this regard, offshore wind energy has been experiencing a promising penetration in both established wind energy markets of Europe and in the emerging markets of Asia. According to the Global Wind Energy Council (GWEC), the overall installation capacity of offshore wind was 23 GW by the end of 2018[1]. While, the current share of offshore wind is only four percent of the total cumulative wind power generation, the GWEC projection shows that its annual installation rate will exceed 6 GW in the near future. The primary motivation behind offshore wind energy development is that the offshore sites are generally characterized by higher and uniform wind speeds, leading to higher capacity factors. In the context of Japan, the "Marine Renewable Energy Utilization Act 2019" was passed in order to accelerate the development of offshore wind energy coastal area[2]. Furthermore, government has designated 11 offshore sites for wind energy development; four of those sites have already seen initial development with the start of planning and site assessments.

Majority of those offshore wind energy developments are planned in the nearshore regions, starting from a few kilometers to 10 to 20 km from shores. Further offshore, water depth can be significant, thus making it less feasible for the fixed-bottom wind turbines. However, power output and loads of wind turbines installed in nearshore regions will be affected by onshore terrain which slow down the wind speed and increase the turbulence level for wind blowing from land to sea. When air flows from land towards sea, it experiences change in surface roughness, and the process is essentially rough-to-smooth surface transition. It has been reported that during the rough-to-smooth surface transition, the initial rough surface flow dictates the rate of diffusion and turbulence level for a considerable distance over the downstream smooth surface[3]. Furthermore, the internal boundary layer (IBL) that develops following a rough-to-smooth transition has slow growth rate, resulting in a slower recovery of the boundary layer. Recently, Goit *et al.*[4] conducted a LiDAR-based measurement campaigns at a test facility 3.5 km offshore from the coast characterized by moderately complex terrain and 50 m tall cliff. The measurement showed that on average the wind blowing from land was 35% lower than that blowing from the sea.   Thus, the effect of onshore terrain to the offshore wind farm near the coast can be significant.

Several studies have investigated the interaction between offshore wind farms and atmospheric boundary layer (ABL) (see e.g. Porte-Agel *et al.*[5]). However, the effect of coastal terrain on the offshore wind farms has not received sufficient attention. The current study emloys large-eddy simulations (LES) to investigate the effect of onshore terrain on the evolution of atmospheric boundary layer (ABL))—when it transitions from land to sea—and evaluate how such transition influence the performance of nearshore offshore wind farms.

2. Numerical Method

The open source CFD software OpenFOAM[6], is employed to perform LES of a neutrally stratified ABL. The governing flow equations are the filtered Navier-Stokes equations given by:

$$\frac{\partial \tilde{u}_i}{\partial x_i} = 0 \tag{1}$$

$$\frac{\partial \tilde{u}_i}{\partial t} + \frac{\partial}{\partial x_j}\left(\tilde{u}_i \tilde{u}_j\right) = -\frac{1}{\rho}\frac{\partial \tilde{p}}{\partial x_i} + \nu \frac{\partial^2 \tilde{u}_i}{\partial x_j^2} + \frac{\partial \tau_{ij}}{\partial x_j} + f_i \tag{2}$$

where $\tilde{u}_i = [\tilde{u}_1, \tilde{u}_2, \tilde{u}_3]$ is the resolved velocity field corresponding to streamwise, vertical and spanwise directions, $\tilde{p}$ is the pressure field, ρ is the air density, ν is kinematic viscosity, τ_{ij} is subgrid-scale
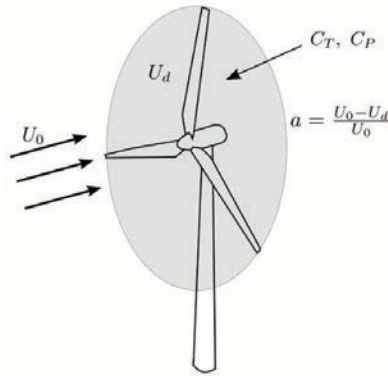

Figure 1: Schematic of the actuator-disk model implementation.

stress. The term f_i represents the force exerted by wind turbine on the flow field and is explained further below. Wall-Adapting Local Eddy-viscosity (WALE) model is employed to model the effect of subgrid-scale stresses on the resolved flow equations[7].

In this study, inlet boundary condition is imposed using the time varying turbulent flow fields which is generated in a separate precursor simulation. The outflow boundary conditions are set to zero-gradient for the velocity and fixed value for the pressure. Slip condition for velocity, and zero-gradient for pressure are applied as the top boundary condition. The spanwise boundary conditions are periodic. The boundary condition at the bottom surface is imposed using a wall stress model which is a function of a velocity field at the first vertical grid point and the surface roughness height. The wall boundary condition enforces constraint on the turbulent viscosity (ν_T) [6].

Force due to wind turbine (f_i) is modelled using actuator-disk model (ADM). Figure 1 shows the schematic of this model implementation. In the ADM, the axial force induced by a wind turbine on the flow is uniformly distributed over a semi-permeable disk. This axial force (F_i) is defined using characteristic thrust coefficient (C_T) of a turbine,

$$F_i = \frac{1}{2} C_T \rho U_0^2 A_d \tag{3}$$

where U_0 is the free stream velocity and $A_d = \pi D^2/4$ is the rotor surface area. Implementation of this model for a lone standing wind turbine is straightforward. For a wind farm however, it is not easy to define

free stream velocities for downstream turbines. To overcome this issue, the proposed model assumes the validity of blade element momentum (BEM) theory for all turbines in a farm. This allows to exploit following relations of axial induction factor (a), C_T and power coefficient (C_P)[8].

$$a = \frac{U_0 - U_d}{U_0}$$

$$C_T = 4a(1 - a) \tag{4}$$

$$C_P = 4a(1 - a)^2$$

where U_d is wind speed at the disk. Since C_T and C_P of the wind turbine, a can be expressed as

$$a = 1 - C_P/C_T, \tag{5}$$

substituting, for a from Eq. (5) into Eq. (4), one can estimate possible free stream velocity from wind speed at the rotor disk, which can be obtained from the simulation. However, in order to avoid numerical oscillation, the thrust force computed using above relations are projected onto simulation grid using Gaussian projection,

$$f_i = \frac{F_i}{\Delta V} \frac{1}{\varepsilon^3 \pi^{3/2}} exp\left(-\frac{r^2}{\varepsilon^2}\right) \tag{6}$$

where ΔV is the volume of simulation grid cell, ε is a filter width and r is the distance between actuator point and the target grid point.

3. Results and Discussions

Four main simulations were performed for this study:
  (i)   Sea-to-land transition of ABL
  (ii) Land-to-sea transition of ABL
  (iii) Wind farm simulation with offshore only condition
  (iv) Wind farm simulation with land-to-sea transition of ABL

Onshore and offshore surfaces are modelled by imposing roughness heights of $z_{0,land} = 0.2$ m and $z_{0,sea} = 0.001$ m, respectively. The size of the computation domain for the simulation cases (i), (ii) and (iv) was $L_x \times L_y \times L_z = 15\text{km} \times 1\text{km} \times 3\text{km}$, while that for the simulation case (iii) was $L_x \times L_y \times L_z = 13\text{km} \times 1\text{km} \times 3\text{km}$. The domain for land-to-sea transition cases (i) & (iv) started with 2 km of land surface and that for sea-to-land transition case (ii) started with 2 km of sea surface. Grid resolutions in streamwise, vertical and spanwise directions are $dx \times dy \times dz = 10$ m $\times 5$ m $\times 8$ m resulting in the total number of grid points of 97.5×10^6 for case (iii) and 11.25×10^7 for other three cases. Wind farm simulations were performed with 50 turbines in 10×5 grid arrangement. Streamwise and spanwise spacing are 7D and 5D respectively, with the rotor diameter (D) being 120 m.

3.1 Atmospheric Boundary Layer Fields

Figure 2 shows vertical profiles of streamwise mean velocity obtained from the ABL simulations. For both roughness height, i.e., $z_{0,land}$ and $z_{0,sea}$, profiles agree with the logarithmic profiles upto the height of 200 m. Above 200 m, gradual increase in the log-lawmismatch can be observed. Note that the vertical line shows the hub height position of the wind turbine simulated in cases (iii) and (iv).
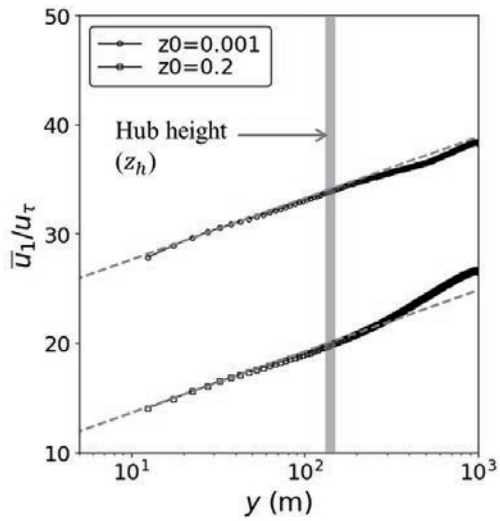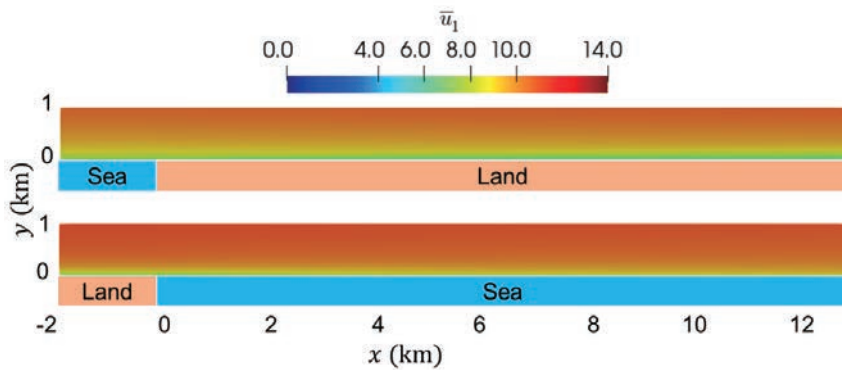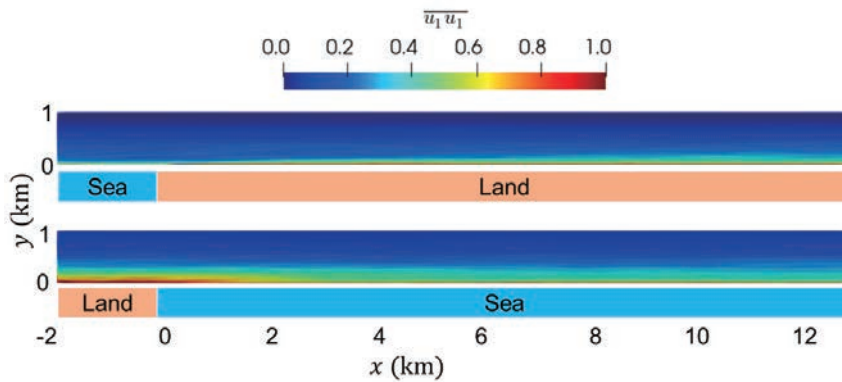
Figure 2: Streamwise mean velocity profiles.

(a) streamwise mean velocities

(b) streamwise component of the normal stresses.

Figure 3: Streamwise-vertical plane showing mean velocities and normal stresses.

Figure 3 shows the streamwise-vertical plane of mean velocity and normal stress fields for ABL

simulations **(Case i and Case ii).** In the mean velocity fields, wind speed in the surface region is slowing down for sea-to-land transition, while it accelerates for land-to-sea transition. This slow down and acceleration can be observed right after the step change in the surface roughness and are essentially the IBL. The downstream evolution of the IBLs are more obvious in normal stress and shear stress (not shown here) fields. Sea-to-land transition, which results into the increase in the surface roughness, increase the turbulence level in the surface region. The normal stress for this case seems to gets higher right from the transition point. For the land-to-sea transition, which results into the drop in the surface roughness, the turbulence level is supposed to decrease after the transition. However, this is happening gradually. The original turbulence level prevails for roughly 2 km even after the transition. Significant amount of turbulence level can be observed in the entire streamwise domain considered in this study. This shows that the onshore turbulence can influence wind farm performance as far as 10 km or more offshore from the coast.

3.2 Wind Farm Simulations

　　Figure 4 compares snapshots of instantaneous velocity fields in hub height and vertical planes for Case iii (offshore only) and Case iv (land-to-sea transition). Wakes from turbines can be observed extending all along the turbine columns with instances of wake meanderings. Flow fields are more turbulent in Case iv. Time-averaged flow fields are compared in 5 which shows contours of mean velocities and streamwise normal stresses in the vertical plane along the rotor center. In addition to the original IBL due to land-to-sea transition, a new IBL develops from the first turbine row in both the cases. Though not quantitatively analyzed, IBL for land-to-sea transition case is slightly thicker. Note that driving pressure in the precursor simulations for both the cases was adjusted such that the mean wind speed in the upper part of the domain would be same in both simulations. The normal stress contours show that turbulence induced by wind farm is significant. Qualitatively, no significant difference in the normal stress evolution for the Case iii and Case iv can be observed. Furthermore, the normal stress due to land to sea transition observed in ABL simulation (see Figure 3 (b)) is not sufficiently large compared to the turbine-induced stresses. Nevertheless, the IBL height is larger for the land-to-sea transition case. This may be because the inflow is more turbulent in the land-to-sea transition case, thus triggering the faster growth of the IBL.

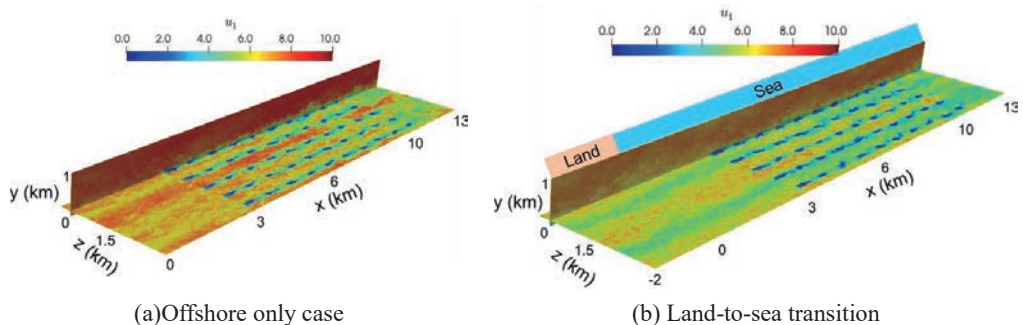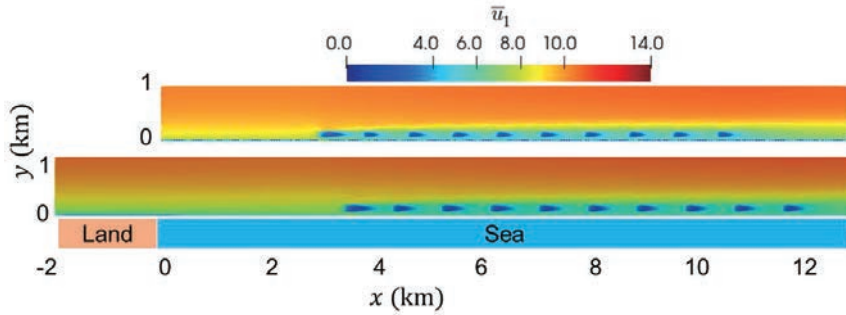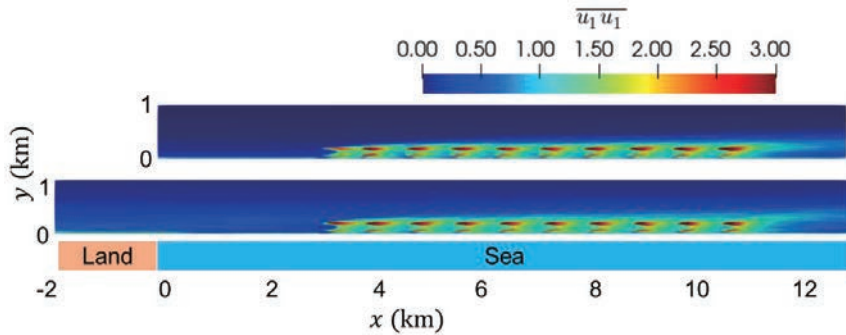(a)Offshore only case　　　　　　　　　　(b) Land-to-sea transition

Figure 4: Instantaneous velocity fields. Horizontal planes are taken along the hub height.

(a) streamwise mean velocities

(b) streamwise component of the normal stresses.

Figure 5: Streamwise-vertical plane showing mean velocities and normal stresses inside the wind farms.

In order to evaluate the effect of land-to-sea transition, we have compaed the time-and-row averaged power output as a function of turbine row in Figure 6. The power has been normalized by the power of the first turbine row from Case iii (offshore only case). It is interesting to observe that although the power output from the first turbine row is slightly higher for offshore only case, for the downstream rows, land-to-sea transition case produce higher power. This normalized power for land-to-sea transition was about 10% higher compared to offshore only case. This may be because higher turbulence in the land-to-sea transition case would improve the energy entrainment from the flow above the wind farm.
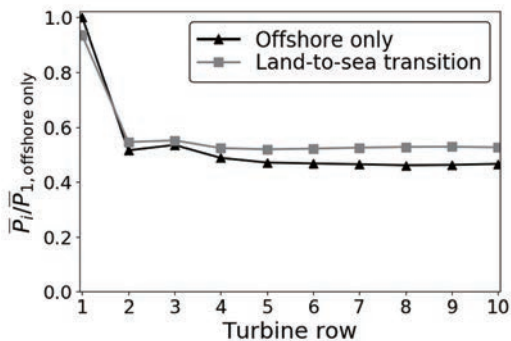

Figure 6: Time-and-row-averaged power output.

4. Summaries

In this study we have investigated the effect of coastal terrain on the performance of nearshore offshore wind farms and flow characteristics inside the farms. To that end, two LES cases were defined using the characteristic surface roughness of land and sea surfaces. In the ABL simulations of land-to-sea transition and sea-to-land transition, internal boundary layer (IBL) could be observed to develop from the point of step change in surface roughness. However, the downstream evolution of the IBL was more obvious in normal and shear stresses fields compared to the mean velocity fields. In the wind farm simulation cases wind farm induced IBL and turbulence were dominant. However, the IBL height was larger for the land-to-sea transition case. This could be attributed to the higher inflow turbulence level in this case. In terms of power output land-to-sea transition case produced 10% higher power. Difference in power output was predominantly observed for downstream rows. This may be due to the fact that the higher inflow turbulence in land-to-sea transition would improve the energy entrainment thus bringing more energy from the flow above in the wind farm region.

References

1. *GWEC Global Wind Report 2019*.; 2019.

2. Ministry of Economy, Trade and Industry:
   https://www.meti.go.jp/press/2019/07/20190730001/20190730001.html.
   https://www.meti.go.jp/press/2019/07/20190730001/20190730001.html. Accessed November 4, 2020.

3. Antonia RA, Luxton RE. The response of a turbulent boundary layer to an upstanding step change in surface roughness. Part 2. Rough-to-smooth. *J Fluids Eng Trans ASME*. 1972;53(4):737-757. doi:10.1115/1.3425174

4. Goit JP, Yamaguchi A, Ishihara T. Measurement and Prediction of Wind Fields at an Offshore Site by Scanning Doppler LiDAR and WRF. *Atmosphere (Basel)*. 2020;2020(11):442. doi:doi:10.3390/atmos11050442

5. Porté-Agel F, Wu YT, Chen CH. A numerical study of the effects of wind direction on turbine wakes and power losses in a largewind farm. *Energies*. 2013;6(10):5297-5313. doi:10.3390/en6105297

6. OpenFOAM. https://www.openfoam.com/. Accessed July 18, 2020.

7. Nicoud F, Ducros F. Subgrid-scale stress modelling based on the square of the velocity. *Flow, Turbul Combust*. 1999;62:183-200. doi:10.1016/j.jcp.2004.10.018

8. Manwell JF, McGowan JG, Rogers AL. *Wind Energy Explained: Theory, Design and Application*.; 2009. doi:10.1002/9781119994367